Prepared for submission to JHEP

First extraction of valence transversities in a collinear framework

Alessandro Bacchetta[a,b] **A. Courtoy**[c,d] **Marco Radici**[b]

[a] *Dipartimento di Fisica, Università di Pavia, via Bassi 6, I-27100 Pavia, Italy*
[b] *INFN Sezione di Pavia, via Bassi 6, I-27100 Pavia, Italy*
[c] *IFPA, AGO Department, Université de Liège, Bât. B5, Sart Tilman B-4000 Liège, Belgium*
[d] *INFN, Laboratori Nazionali di Frascati, Via E. Fermi, 40, I-00044 Frascati (Roma), Italy*

E-mail: alessandro.bacchetta@unipv.it, aurore.courtoy@ulg.ac.be, marco.radici@pv.infn.it

Abstract: We present an extraction of the valence transversity parton distributions based on an analysis of pion-pair production in deep-inelastic scattering off transversely polarized targets. Recently released data for proton and deuteron targets at HERMES and COMPASS permit a flavor separation of valence transversities. The present extraction is performed in the framework of collinear factorization, where dihadron fragmentation functions are involved. The latter are taken from a previous analysis of electron-positron annihilation measurements.

Contents

1 Introduction

The distribution of quarks and gluons inside hadrons can be described by means of parton distribution functions (PDFs). In a parton model picture, PDFs describe combinations of number densities of quarks and gluons in a fast-moving hadron. The knowledge of PDFs is crucial for our understanding of QCD and for the interpretation of high-energy experiments involving hadrons. At leading twist, the quark structure of spin-half hadrons is described by three PDFs: the unpolarized distribution $f_1(x)$, the longitudinal polarization (helicity) distribution $g_1(x)$, and the transverse polarization (transversity) distribution $h_1(x)$ [**?** **?** **?** **?**]. From the phenomenological point of view, the unpolarized PDFs are well-known, as can be evinced by the large number of parametrizations available (see, *e.g.*, Ref. [**?**] and references therein). Apart from giving us invaluable information about the structure of nucleons, they have a fundamental importance for the interpretation of measurements in any hadronic colliders, *e.g.*, the LHC. The helicity PDFs are known to some extent, see *e.g.* Refs. [**?** **?** **?** **?**]. On the other hand, the transversity distribution is poorly known (see, *e.g.*, Refs. [**?**] and references therein). This is mainly due to the fact that transversity can be measured only in processes with two hadrons in the initial state [**?**], *e.g.* proton-proton collision, or one hadron in the initial state and at least one hadron in the final state, *e.g.* semi-inclusive DIS (SIDIS).

Combining data from HERMES [**?**] and COMPASS [**?**] on polarized SIDIS with one hadron in the final state, together with data from Belle [**?**] on almost back-to-back emission of two hadrons in e^+e^- annihilations, the transversity distribution was extracted for the first time by the Torino group [**?**]. The main difficulty of such analysis lies in the factorization framework used to interpret the data, since they involve Transverse Momentum Dependent

PDFs (TMDs). In spite of exceptional progress in the understanding of TMDs [**? ? ? ? ? ?**], we have still limited information on their evolution equations, which are needed when analyzing measurements at very different scales.

In this paper, we extract the transversity distribution for the valence combination of up and down quarks, applying for the first time an approach based on standard collinear factorization. We use data on SIDIS with two hadrons detected in the final state, where the transversity distribution is combined with the so-called Dihadron Fragmentation Functions (DiFFs) [**? ? ?**]. The collinear framework allows us to keep under control the evolution equations of DiFFs [**?**].

In Sec. 2, we summarize the theoretical framework for two-hadron SIDIS. The parametrization of the valence transversity and its error analysis is described in Sec. 3. The results are discussed in Sec. 4. We finally illustrate the possible applications and extensions of our analysis and draw our conclusions in Sec. 5.

2 Theoretical framework for two-hadron SIDIS

We consider the process

$$\ell(k) + N(P) \to \ell(k') + H_1(P_1) + H_2(P_2) + X \ , \tag{2.1}$$

where ℓ denotes the beam lepton, N the nucleon target, H_1 and H_2 the produced hadrons, and where four-momenta are given in parentheses. We work in the one-photon exchange approximation and neglect the lepton mass. We denote by M the mass of the nucleon and by S its polarization. The final (unpolarized) hadrons, with mass M_1, M_2 and momenta P_1, P_2, have invariant mass squared $P_h^2 = M_h^2$ (which we consider much smaller than the hard scale $Q^2 = -q^2 \geq 0$ of the SIDIS process). The $P_h = P_1 + P_2$ is the total momentum of the pair; we define also its relative momentum $R = (P_1 - P_2)/2$. The momentum transferred to the nucleon target is $q = k - k'$. The kinematics of the process is depicted in Fig. 1 (see also Ref. [**?**]).

The component $\boldsymbol{S}_T$ of the target polarization is transverse to both the virtual-photon and target momenta $\boldsymbol{q}$ and $\boldsymbol{P}$, respectively. Instead, $\boldsymbol{R}_T = \boldsymbol{R} - (\boldsymbol{R}\cdot\hat{\boldsymbol{P}}_h)\hat{\boldsymbol{P}}_h$ is orthogonal to $\hat{\boldsymbol{P}}_h$ but, up to subleading-twist corrections, it can be identified with its projection on the plane perpendicular to $\boldsymbol{q}$ and containing also $\boldsymbol{S}_T$. The azimuthal angle ϕ_R is the angle of $\boldsymbol{R}_T$ about the virtual-photon direction; similarly for the azimuthal angle ϕ_S of $\boldsymbol{S}_T$. The explicit expressions are

$$\begin{aligned}
\phi_R \equiv & \frac{(\boldsymbol{q}\times\boldsymbol{k})\cdot\boldsymbol{R}_T}{|(\boldsymbol{q}\times\boldsymbol{k})\cdot\boldsymbol{R}_T|}\arccos\frac{(\boldsymbol{q}\times\boldsymbol{k})\cdot(\boldsymbol{q}\times\boldsymbol{R}_T)}{|\boldsymbol{q}\times\boldsymbol{k}||\boldsymbol{q}\times\boldsymbol{R}_T|} \ , \\
\phi_S \equiv & \frac{(\boldsymbol{q}\times\boldsymbol{k})\cdot\boldsymbol{S}_T}{|(\boldsymbol{q}\times\boldsymbol{k})\cdot\boldsymbol{S}_T|}\arccos\frac{(\boldsymbol{q}\times\boldsymbol{k})\cdot(\boldsymbol{q}\times\boldsymbol{S}_T)}{|\boldsymbol{q}\times\boldsymbol{k}||\boldsymbol{q}\times\boldsymbol{S}_T|} \ .
\end{aligned} \tag{2.2}$$

We also define the polar angle θ which is the angle between the direction of the back-to-back emission in the center-of-mass (cm) frame of the two hadrons, and the direction of P_h in

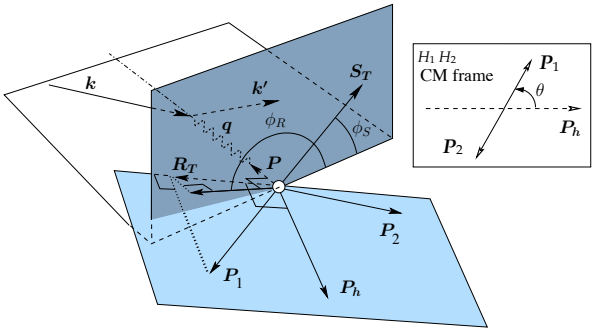

Figure 1. Kinematics of the two-hadron semi-inclusive production. The azimuthal angles ϕ_R of the dihadron, and ϕ_S of the component $\boldsymbol{S}_T$ of the target-polarization, transverse to both the virtual-photon and target-nucleon momenta $\boldsymbol{q}$ and $\boldsymbol{P}$, respectively, are evaluated in the virtual-photon-nucleon center-of-momentum frame.

the photon-proton cm frame (see Fig. 1). We have

$$|\boldsymbol{R}| = \frac{1}{2}\sqrt{M_h^2 - 2(M_1^2+M_2^2) + (M_1^2-M_2^2)^2/M_h^2}\,,$$
$$\boldsymbol{R}_T = \boldsymbol{R}\sin\theta\,. \tag{2.3}$$

As usual in SIDIS, we define also the following kinematic invariants

$$x = \frac{Q^2}{2\,P\cdot q}\,, \quad y = \frac{P\cdot q}{P\cdot k}\,, \quad \gamma = \frac{2Mx}{Q}\,, \tag{2.4}$$

$$z = \frac{P\cdot P_h}{P\cdot q} \equiv z_1 + z_2\,, \quad \zeta = \frac{z_1 - z_2}{z}\,, \tag{2.5}$$

where z_1, z_2, are the fractional energies carried by the two final hadrons. The invariant ζ can be shown to be a linear polynomial in $\cos\theta$ [**?**].

To leading order in the couplings and leading twist, the differential cross section for the two-hadron SIDIS of an unpolarized lepton off a transversely polarized nucleon target contains only two nonvanishing structure functions:

$$\frac{d\sigma}{dx\,dy\,d\psi\,dz\,d\phi_R\,dM_h^2\,d\cos\theta} =$$
$$\frac{\alpha^2}{xy\,Q^2}\,\frac{y^2}{2\,(1-\varepsilon)}\left(1+\frac{\gamma^2}{2x}\right)\left\{F_{UU} + |\boldsymbol{S}_T|\,\varepsilon\,\sin(\phi_R+\phi_S)\,F_{UT}^{\sin(\phi_R+\phi_S)}\right\}, \tag{2.6}$$

where α is the fine structure constant and the structure functions F depend on x, Q^2, z, $\cos\theta$, and M_h. The first and second subscripts of F indicate the polarization of beam and target, respectively. Here, the target polarization refers to the virtual-photon direction; the conversion to the experimental polarization with respect to the lepton beam is straightforward and given in Ref. [**?**]. The angle ψ is the azimuthal angle of ℓ' around the lepton beam axis with respect to an arbitrary fixed direction, which in case of a transversely polarized

target we choose to be the direction of S. The corresponding relation between ψ and ϕ_S is given in Ref. [**?**]; in DIS kinematics it turns out $d\psi \approx d\phi_S$.

The ratio ε of longitudinal and transverse photon flux in Eq. (2.6) is given by [**?**]

$$\varepsilon = \frac{1 - y - \frac{1}{4}\gamma^2 y^2}{1 - y + \frac{1}{2}y^2 + \frac{1}{4}\gamma^2 y^2} \,, \tag{2.7}$$

so that the depolarization factors can be written as

$$\begin{aligned} \frac{y^2}{2\,(1-\varepsilon)} &= \frac{1}{1+\gamma^2}\left(1 - y + \tfrac{1}{2}y^2 + \tfrac{1}{4}\gamma^2 y^2\right) \approx \left(1 - y + \tfrac{1}{2}y^2\right) \equiv A(y) \,, \\ \frac{y^2}{2\,(1-\varepsilon)}\,\varepsilon &= \frac{1}{1+\gamma^2}\left(1 - y - \tfrac{1}{4}\gamma^2 y^2\right) \qquad \approx (1-y) \qquad\quad \equiv B(y) \,. \end{aligned} \tag{2.8}$$

The ε turns out to be also the ratio between the two depolarization factors: $\varepsilon = B(y)/A(y)$. Neglecting target-mass corrections, we will assume that in each experimental bin

$$\begin{gathered} \langle A(y)\rangle \approx A(\langle y\rangle) \,, \quad \langle B(y)\rangle \approx B(\langle y\rangle) \,, \\ \varepsilon \approx \frac{B(\langle y\rangle)}{A(\langle y\rangle)} \equiv C_y \,. \end{gathered} \tag{2.9}$$

In the limit $M_h^2 \ll Q^2$, the structure functions can be written as products of PDFs and DiFFs [**?** **?** **?**][1]

$$F_{UU} = x \sum_q e_q^2\, f_1^q(x;Q^2)\, D_1^q\big(z, \cos\theta, M_h; Q^2\big) \,, \tag{2.10}$$

$$F_{UT}^{\sin(\phi_R+\phi_S)} = \frac{|\boldsymbol{R}|\sin\theta}{M_h}\, x \sum_q e_q^2\, h_1^q(x;Q^2)\, H_1^{\sphericalangle\, q}\big(z, \cos\theta, M_h; Q^2\big) \,, \tag{2.11}$$

where e_q is the fractional charge of a parton with flavor q. The D_1^q is the unpolarized DiFF describing the hadronization of a parton with flavor q into an unpolarized hadron pair plus anything else, averaging over the parton polarization. The $H_1^{\sphericalangle\, q}$ is a chiral-odd DiFF describing the correlation between the transverse polarization of the fragmenting parton with flavor q and the azimuthal orientation of the plane containing the momenta of the detected hadron pair.

For $M_h \ll Q$, the hadron pair can be assumed to be produced mainly in relative s or p waves, suggesting that the DiFFs can be conveniently expanded in partial waves. In the two-hadron cm frame, the relevant changes in the kinematics are summarized in Eq. (2.3). From the simple relation between ζ and $\cos\theta$, DiFFs can be expanded in Legendre polynomials in $\cos\theta$ as [**?**]

$$\begin{aligned} D_1 &\to D_{1,ss+pp} + D_{1,sp}\cos\theta + D_{1,pp}\frac{1}{4}\left(3\cos^2\theta - 1\right) \,, \\ H_1^{\sphericalangle} &\to H_{1,sp}^{\sphericalangle} + H_{1,pp}^{\sphericalangle}\cos\theta \,. \end{aligned} \tag{2.12}$$

[1] For some discussion of the case $M_h^2 \approx Q^2$, see Ref. [**?**]

All the $\cos\theta-$dependent terms disappear after integrating upon $d\cos\theta$; they still vanish even if the θ dependence of the acceptance is not complete but symmetric about $\theta = \pi/2$. Of the remaining terms, the subscript $ss + pp$ refers to the unpolarized pair being created in a relative $\Delta L = 0$ state, while sp indicates the interference in $|\Delta L| = 1$. For simplicity, we will use the notation $D_{1,ss+pp} \equiv D_1$ since no ambiguity arises in the following.

From the cross section of Eq. (2.6), and by inserting the structure functions of Eqs. (2.10), (2.11) with the approximation of Eq. (2.12), we obtain the following single-spin asymmetry (SSA) [**? ? ?**]

$$\begin{aligned}
&A_{UT}^{\sin(\phi_R+\phi_S)\,\sin\theta}(x,z,M_h;Q) = \\
&= \frac{1}{|\boldsymbol{S}_T|}\,\frac{\frac{8}{\pi}\int d\phi_R\, d\cos\theta\, \sin(\phi_R+\phi_S)\,(d\sigma^{\uparrow}-d\sigma^{\downarrow})}{\int d\phi_R\, d\cos\theta\,(d\sigma^{\uparrow}+d\sigma^{\downarrow})} = \frac{\frac{4}{\pi}\,\varepsilon\int d\cos\theta\, F_{UT}^{\sin(\phi_R+\phi_S)}}{\int d\cos\theta\, F_{UU}} \\
&= -C_y\,\frac{|\boldsymbol{R}|}{M_h}\,\frac{\sum_q e_q^2\, h_1^q(x;Q^2)\, H_{1,sp}^{\sphericalangle\, q}(z,M_h;Q^2)}{\sum_q e_q^2\, f_1^q(x;Q^2)\, D_1^q(z,M_h;Q^2)} \\
&\equiv A_{\rm SIDIS}\,. \qquad (2.13)
\end{aligned}$$

We are interested in the specific case of semi-inclusive production of $\pi^+\pi^-$ pairs. Then, isospin symmetry and charge conjugation suggest [**? ?**]

$$D_1^u = D_1^{\bar u}\,, \quad D_1^d = D_1^{\bar d}\,, \quad D_1^s = D_1^{\bar s}\,, \qquad (2.14)$$

$$H_1^{\sphericalangle\, u} = -H_1^{\sphericalangle\, d} = -H_1^{\sphericalangle\, \bar u} = H_1^{\sphericalangle\, \bar d}\,, \quad H_1^{\sphericalangle\, s} = -H_1^{\sphericalangle\, \bar s} = 0\,. \qquad (2.15)$$

For a proton target, the SSA (2.13) simplifies to [**? **]

$$\begin{aligned}
&A_{\rm SIDIS}^{p}(x,z,M_h;Q^2) = \\
&\quad - C_y\,\frac{|\boldsymbol{R}|}{M_h} H_{1,sp}^{\sphericalangle\, u}(z,M_h;Q^2)\,\left[h_1^{u_v}(x;Q^2) - \tfrac{1}{4} h_1^{d_v}(x;Q^2)\right] \\
&\quad \times \Big\{ f_1^{u+\bar u}(x;Q^2)\, D_1^u(z,M_h;Q^2) + \tfrac{1}{4} f_1^{d+\bar d}(x;Q^2)\, D_1^d(z,M_h;Q^2) \\
&\qquad + \tfrac{1}{4}\, f_1^{s+\bar s}(x)\, D_1^{s+\bar s}(z,M_h;Q^2)\Big\}^{-1}\,, \qquad (2.16)
\end{aligned}$$

and for a deuteron target to

$$\begin{aligned}
&A_{\rm SIDIS}^{D}(x,y,z,M_h;Q^2) = \\
&\quad - C_y\,\frac{3}{4}\,\frac{|\boldsymbol{R}|}{M_h} H_{1,sp}^{\sphericalangle\, u}(z,M_h;Q^2)\,\left[h_1^{u_v}(x;Q^2) + h_1^{d_v}(x;Q^2)\right] \\
&\quad \times \Big\{ \left[f_1^{u+\bar u}(x;Q^2) + f_1^{d+\bar d}(x;Q^2)\right]\,\left[D_1^u(z,M_h;Q^2) + \tfrac{1}{4}\, D_1^d(z,M_h;Q^2)\right] \\
&\qquad + \tfrac{1}{2}\, f_1^{s+\bar s}(x;Q^2)\, D_1^{s+\bar s}(z,M_h;Q^2)\Big\}^{-1}\,, \qquad (2.17)
\end{aligned}$$

where $h_1^{q_v} \equiv h_1^q - h_1^{\bar q}$ and $f_1^{q+\bar q} \equiv f_1^q + f_1^{\bar q}$.

Eqs. (2.16) and (2.17) contains two sets of unknowns: the transversity h_1 (in various flavor combinations) and the DiFFs. Before the measurement by the Belle collaboration of the angular distribution of two pion pairs produced in e^+e^- annihilations [**?**], the only information available on DiFFs were coming from model calculations in the context of the spectator approximation [**?** **?** **?**] (and, recently, also using the NJL-jet model [**?**]). The unpolarized D_1 was tuned to the Monte Carlo event generator [**?**] and the polarized $H_{1\,sp}^{\sphericalangle}$ compared to the asymmetry measured by the HERMES collaboration in SIDIS on proton targets [**?**], the only available set of experimental data at that time [**?**].

The first analysis of the so-called Artru–Collins asymmetry [**?**] in e^+e^- annihilations by the Belle collaboration made possible a direct extraction of $H_{1\,sp}^{\sphericalangle}$ for the production of $\pi^+\pi^-$ pairs. In the absence of a measurement of the unpolarized e^+e^- cross section (planned at Belle in the near future), D_1 was parametrized to reproduce the two-hadron yield of the PYTHIA event generator, which is known to give a good description of data. Combining such a parametrization with the fit of the azimuthal asymmetry presented in Ref. [**?**], it was possible to extract for the first time the $H_{1\,sp}^{\sphericalangle}$ [**?**].

The knowledge of DiFFs in Eq. (2.16) allowed us to get a glimpse of the combination $h_1^{u_v} - h_1^{d_v}/4$ directly from the HERMES data for $A^p_{\rm SIDIS}$ [**?**]. The effects produced by evolving DiFFs between the HERMES and Belle very different scales were properly included by using standard evolution equations in a collinear framework [**?**] and by implementing leading-order (LO) chiral-odd splitting functions in the HOPPET code [**?**]. Recently, the COMPASS collaboration has released new data for $A^p_{\rm SIDIS}$ on a proton target and for $A^D_{\rm SIDIS}$ on a deuteron target, with higher statistics and wider kinematic coverage [**?**]. Thus, the combination of SSA of Eqs. (2.16) and (2.17) makes it possible to separately parametrize each valence flavor of the transversity distribution, which we present here for the first time (see also Ref. [**?**] for a first attempt to obtain a flavor separation point by point).

In the collinear framework, the dependence of the SSA on the momentum fraction x gets factorized from the dependence on (z, M_h), as it is evident in Eqs. (2.16) and (2.17). This suggests that the dependence of the SSA on x comes only from the involved PDFs. Therefore, it is more convenient to study it by integrating the z- and M_h-dependence of DiFFs. Then, the actual combinations of transversity used in the analysis are, for the proton,

$$
\begin{aligned}
x\,h_1^p(x;Q^2) &\equiv x\,h_1^{u_v}(x;Q^2) - \tfrac{1}{4}\,x h_1^{d_v}(x;Q^2) \\
&= -\frac{A^p_{\rm SIDIS}(x;Q^2)}{C_y\,n_u^{\uparrow}(Q^2)} \\
&\quad\times\left[n_u(Q^2)\,x f_1^{u+\bar u}(x;Q^2) + \tfrac{1}{4}\,n_d(Q^2)\,x f_1^{d+\bar d}(x;Q^2) + \tfrac{1}{4}\,n_s(Q^2)\,x f_1^{s+\bar s}(x;Q^2)\right],
\end{aligned}
\tag{2.18}
$$

and, for the deuteron,

$$
\begin{aligned}
x\,h_1^D(x;Q^2) &\equiv x\,h_1^{u_v}(x;Q^2) + x h_1^{d_v}(x;Q^2) \\
&= -\frac{A^D_{\rm SIDIS}(x;Q^2)}{C_y\,n_u^{\uparrow}(Q^2)}\frac{4}{3} \\
&\quad\times\left[\left(x f_1^{u+\bar u}(x;Q^2) + x f_1^{d+\bar d}(x;Q^2)\right)\left(n_u(Q^2) + \frac{n_d(Q^2)}{4}\right) + \frac{n_s(Q^2)}{2}\,x f_1^{s+\bar s}(x;Q^2)\right],
\end{aligned}
\tag{2.19}
$$

where

$$
n_q(Q^2) = \int_{z_{\rm min}}^{z_{\rm max}}\int_{M_{h\,\rm min}}^{M_{h\,\rm max}} dz\,dM_h\,D_1^q(z,M_h;Q^2)\,, \tag{2.20}
$$

$$
n_q^{\uparrow}(Q^2) = \int_{z_{\rm min}}^{z_{\rm max}}\int_{M_{h\,\rm min}}^{M_{h\,\rm max}} dz\,dM_h\,\frac{|\boldsymbol{R}|}{M_h}\,H_{1\,sp}^{\sphericalangle\,q}(z,M_h;Q^2)\,. \tag{2.21}
$$

Using the unpolarized PDFs from the MSTW08LO set [**?**], early explorations were presented in Ref. [**?**].

3 Fitting procedure

Here, we describe our fitting procedure to obtain the valence transversity distribution functions for up and down quarks. We discuss first the choice of the functional form.

The main theoretical constraint we have is Soffer's inequality [**?**] (see also [**?**])

$$
2|h_1^q(x;Q^2)| \le |f_1^q(x;Q^2) + g_1^q(x;Q^2)| \equiv 2\,{\rm SB}^q(x;Q^2)\,. \tag{3.1}
$$

We impose this condition by multiplying the functional form by the corresponding Soffer bound at the starting scale of the parameterization. If the Soffer bound is fulfilled at some initial Q_0^2, it will hold also at higher $Q^2 \ge Q_0^2$ [**?** **?**]. The implementation of the Soffer bound depends on the choice of the unpolarized and helicity PDFs. We use the MSTW08 set [**?**] for the unpolarized PDF, combined to the DSSV parameterization [**?**] for the helicity distribution, at the scale of $Q_0^2 = 1$ GeV^2. Our analysis was carried out at LO in α_S. To be as consistent as possible, we decided to use the MSTW08LO set for f_1 and the DSSV set for g_1, even if the DSSV fit provides only a NLO parametrization of g_1. For convenience, in App. A we list the explicit form of ${\rm SB}^q$. The result for the Soffer bound is affected by an error coming mainly from the uncertainty in the knowledge of the helicity PDF g_1. We checked that at the explored hard scales this error is much smaller than the experimental errors on $A_{\rm SIDIS}$ data and the statistical error on the DiFF parametrization; hence, we will neglect it.

The Soffer bound is valid for each quark and antiquark. Since we need to parametrize the transversity valence combinations for up and down quarks, we have necessarily to constrain it by taking the sum of Soffer bounds for both quarks and antiquarks. This likely leads to a loose bound, especially at low x. In particular, due to the divergent behavior of PDFs the "valence" Soffer bound is not even integrable in the range $x \in [0,1]$, which would

result in a divergent tensor charge. Given the chosen analytical form of the PDFs at low x, the SB^q has to be multiplied by at least $x^{0.16276}$.

Based on the above considerations, we adopted the following functional form for the valence transversity distributions at $Q_0^2 = 1$ GeV^2:

$$x\,h_1^{q_V}(x;Q_0^2) = \tanh\Big[x^{1/2}\left(A_q + B_q\,x + C_q\,x^2 + D_q\,x^3\right)\Big]\,\Big[x\,\mathrm{SB}^q(x;Q_0^2) + x\,\mathrm{SB}^{\bar{q}}(x;Q_0^2)\Big]\ . \quad (3.2)$$

The hyperbolic tangent is such that the Soffer bound is always fulfilled. The functional form is very flexible and can contain up to three nodes. The low-x behavior is however determined by the $x^{1/2}$ term, which is imposed by hand. Present fixed-target data do not allow to constrain it.

The fit, and in particular the error analysis, was carried out in two different ways: using the standard Hessian method and using a Monte Carlo approach. As usual, we remind the reader that both methods are suitable to estimate the errors of statistical nature only, assuming a specific choice of the theoretical function. Care must be taken especially when using error bands outside the region where data exist.

The standard fitting procedure consists in minimizing the usual χ^2 function, defined as

$$\chi^2(\{p\}) = \sum_i \frac{\Big(x_i\,h_{1,\mathrm{data}}^{p/D}(x_i;Q_i^2) - x_i\,h_{1,\mathrm{theo}}^{p/D}(x_i,Q_i^2;\{p\})\Big)^2}{\Big(\Delta h_{1,\mathrm{data}}^{p/D}(x_i;Q_i^2)\Big)^2}\ , \quad (3.3)$$

where the sum runs over the experimental points, the expressions for $x\,h_1^{p/D}$ are listed in Eqs. (2.18) and (2.19), and $\{p\}$ denotes the vector of parameters. The evolution of the functional form (3.2) to the values Q_i^2 for each data bin has been implemented using the HOPPET code [**?**], set to the $\overline{\mathrm{MS}}$ renormalization scheme and modified to include also the LO chiral-odd splitting functions needed for transversity evolution. The input value for the running coupling constant at $Q_0^2 = 1$ GeV^2 is chosen to be the best-fit value of the MSTW08LO set, i.e. $\alpha_S^{\mathrm{LO}}(Q_0^2) = 0.13939$. It is true for all the evolved quantities of our analysis, including the Soffer bound. The minimization has been carried out using the MINUIT code and led to a vector of best-fit parameters, $\{p_0\}$ (and a covariance matrix).

The standard method allows to compute the errors on any theoretical quantity under the assumption that the parameter dependence of χ^2 can be approximated by a quadratic expansion around the minimum, and the parameter dependence of the theoretical quantity can be approximated by a linear expansion around the minimum.

For the standard method, the error on the extracted transversity was estimated using the formula

$$\Big(\Delta h_1(x,Q^2;\{p\})\Big)^2 = \sum_{i,j}^{N_p} \frac{\partial h_{1,\mathrm{theo}}(x,Q^2;\{p\})}{\partial p_i}\Big|_{\{p_0\}}\,\mathrm{Cov}_{ij}\,\frac{\partial h_{1,\mathrm{theo}}(x,Q^2;\{p\})}{\partial p_j}\Big|_{\{p_0\}}\ , \quad (3.4)$$

where N_P is the number of parameters. The covariance matrix Cov_{ij} has been obtained using the condition $\Delta\chi^2 = 1$. Therefore, within the limits of applicability of the standard approach, the obtained error band corresponds to the 1σ or 68% confidence level. In typical

PDF global fits, often the value of $\Delta\chi^2$ is increased of one or even two orders of magnitude, with a corresponding increase in the error estimate (see, e.g., [**?**]). In the present analysis, we find no need of such an increase, as demonstrated by the agreement with the Monte Carlo approach.

The Monte Carlo approach does not rely on the assumptions of a quadratic dependence of χ^2 and a linear expansion of the theoretical quantity around $\{p_0\}$, respectively. In our case, the need of such an approach is essential whenever the minimization pushes the theoretical functions towards their upper or lower bounds, where it is not possible to assume a simple linear expansion in the parameters.

For the implementation of this approach, we took inspiration from the work of the NNPDF collaboration (see, e.g., [**? ? ?**]), although our results are not based on a neural-network fit. The approach consists in creating N replicas of the data points. In each replica (denoted by the index r), each data point i is shifted by a Gaussian noise with the same variance as the measurement. Each replica, therefore, represents a possible outcome of an independent experimental measurement, which we denote by $h_{1,r}^{p/D}(x_i;Q_i^2)$. The number of replicas is chosen so that the mean and standard deviation of the set of replicas accurately reproduces the original data points. In our case, we have found that 100 replicas are sufficient.

The standard minimization procedure is applied to each replica separately, by minimizing the following error function[2]

$$E_r^2(\{p\}) = \sum_i \frac{\left(x_i\, h_{1,r}^{p/D}(x_i;Q_i^2) - x_i\, h_{1,\mathrm{theo}}^{p/D}(x_i,Q_i^2;\{p\})\right)^2}{\left(\Delta h_{1,\mathrm{data}}^{p/D}(x_i;Q_i^2)\right)^2}\,, \tag{3.5}$$

resulting in N different vectors of best-fit parameter values, $\{p_{0r}\}$, $r = 1,\dots N$. These parameter vectors can be used to produce N values for any theoretical quantity. The N theoretical outcomes can have any distribution, not necessarily Gaussian. For non-Gaussian distributions, the 1σ confidence interval is in general different from the 68% interval. Both of them can be easily computed from the N theoretical outcomes. For instance, for the 68% interval we simply take for each experimental point i the N values and we reject the largest and the lowest 16% of them.

Although the minimization is performed on the function defined in Eq. (3.5), the agreement of the N theoretical outcomes with the original data is better expressed in terms of the original χ^2 function defined in Eq. (3.3), i.e. with respect to the original data set without the Gaussian noise. If the model is able to give a good description of the data, the distribution of the N values of χ^2/d.o.f. should be peaked at around one. In real situations, the rigidity of the model shifts the position of the peak to higher values of χ^2/d.o.f..

In our case, we determined $N = 100$ best-fit parameter vectors and we used them to produce 100 curves for the up and down valence transversity. Each one of the resulting

[2]Note that the error for each replica is taken to be equal to the error on the original data points. This is consistent with the fact that the variance of the N replicas should reproduce the variance of the original data points.

HERMES		data		
x	y	$Q^2[\mathrm{GeV}^2]$	A_{SIDIS}	$h_1^{u_v} - h_1^{d_v}/4$
0.033	0.734	1.232	0.015 ± 0.010	0.086 ± 0.061
0.047	0.659	1.604	0.002 ± 0.011	0.010 ± 0.054
0.068	0.630	2.214	0.035 ± 0.011	0.167 ± 0.069
0.133	0.592	4.031	0.020 ± 0.010	0.092 ± 0.054
COMPASS		proton	data	
x		$Q^2[\mathrm{GeV}^2]$	A_{SIDIS}	$h_1^{u_v} - h_1^{d_v}/4$
0.0065		1.232	0.026 ± 0.030	0.10 ± 0.12
0.0105		1.476	0.010 ± 0.016	0.038 ± 0.059
0.0164		1.744	0.015 ± 0.013	0.057 ± 0.049
0.1330		2.094	0.008 ± 0.010	0.031 ± 0.039
0.0398		2.802	0.027 ± 0.011	0.107 ± 0.049
0.0626		4.342	0.029 ± 0.014	0.118 ± 0.060
0.1006		6.854	0.051 ± 0.016	0.208 ± 0.079
0.1613		10.72	0.108 ± 0.023	0.42 ± 0.12
0.2801		21.98	0.080 ± 0.033	0.24 ± 0.11
COMPASS		deuteron	data	
x		$Q^2[\mathrm{GeV}^2]$	A_{SIDIS}	$h_1^{u_v} + h_1^{d_v}$
0.0064		1.253	0.005 ± 0.024	0.05 ± 0.24
0.0105		1.508	-0.004 ± 0.012	-0.04 ± 0.12
0.0163		1.792	0.028 ± 0.010	0.28 ± 0.11
0.0253		2.266	-0.005 ± 0.009	-0.051 ± 0.094
0.0396		3.350	0.006 ± 0.011	0.06 ± 0.12
0.0623		5.406	-0.006 ± 0.014	-0.06 ± 0.14
0.0996		8.890	-0.029 ± 0.019	-0.30 ± 0.20
0.1597		15.65	-0.017 ± 0.030	-0.16 ± 0.28
0.2801		33.22	0.078 ± 0.054	0.50 ± 0.36

Table 1. HERMES data for $\pi^+\pi^-$ production in SIDIS off a transversly polarized proton [**?**] and COMPASS data for the same process off a transversly polarized proton and deuteron [**?**]. The last column shows the combinations of valence transversities obtained using Eqs. (2.18) and (2.19).

curves respects the Soffer bound by construction. The results are discussed in the next section.

4 Results and discussion

In the following, we discuss the results obtained by fitting the expressions of Eqs. (2.18) and (2.19) when inserting the HERMES and COMPASS measurements for the single-spin asymmetries A^p_{SIDIS} and A^D_{SIDIS} on $\pi^+\pi^-$ SIDIS production off transversely polarized proton and deuteron targets, respectively. By combining the two fits, we can determine for each valence flavor u_v and d_v the vector of fitting parameters that gives the corresponding transversity distribution, according to Eq. (3.2).

As discussed in the previous section, the error analysis has been performed in two ways: using the standard Hessian method summarized in Eqs. (3.3) and (3.4), or the Monte Carlo

approach by fitting $N = 100$ replicas of the experimental points according to Eq. (3.5). For each strategy, we explored three different scenarios in the parametrization (3.2) of the transversity distribution:

- the *rigid* scenario, described by the choice $C_u = C_d = D_u = D_d = 0$, i.e. with only 4 free parameters;
- the *flexible* scenario, with $D_u = D_d = 0$ (6 free parameters);
- the *extra-flexible* scenario, with all 8 free parameters.

4.1 Experimental data

In Tab. 1, we list the data for the asymmetries $A^p_{\rm SIDIS}$ and $A^D_{\rm SIDIS}$ of Eqs. (2.16) and (2.17), as they were measured by the HERMES [**?**] and COMPASS [**?**] collaborations in the $\pi^+\pi^-$ SIDIS production off transversely polarized proton and deuteron targets, respectively. The first three columns indicate the average values of the corresponding kinematic variables in each experimental bin. The indicated errors include statistical and systematic contributions added in quadrature. The depolarization factor C_y in the expression of the asymmetries depends on the average y according to Eq. (2.9). In its analysis, the COMPASS collaboration already divided the C_y factor out of the measured cross section; as such, the SSA does no longer depend on y and, correspondingly, there are no y values in the second column of Tab. 1 for COMPASS. Consistently, we have used $C_y = 1$ when fitting the COMPASS data.

The last column in Tab. 1 contains the values of the combination in Eq. (2.18) for the proton target, and of Eq. (2.19) for the deuteron target, when the corresponding experimental values for the SSA are inserted in $A^p_{\rm SIDIS}$ and $A^D_{\rm SIDIS}$, respectively. As already anticipated in the previous sections, for the unpolarized PDFs we adopted the MSTW08LO set [**?**]. The remaining ingredients in Eqs. (2.18) and (2.19) are the n_q and $n_q^\uparrow$ defined in Eqs. (2.20) and (2.21), where the DiFFs D_1^q and $H_{1\,sp}^{\sphericalangle\,q}$ are parametrized as in Ref. [**?**]. The integrals are evaluated according to the appropriate experimental cuts: $0.2 < z < 1$ and $0.5\ {\rm GeV} < M_h < 1\ {\rm GeV}$ for HERMES, $0.2 < z < 1$ and $0.29\ {\rm GeV} < M_h < 1.29\ {\rm GeV}$ for COMPASS. In Tab. 2, the results are given for the relevant flavors at the average scales Q_i^2 for each experimental bin i. The statistical error is indicated only for $n_u^\uparrow$, since the large statistics achievable in the Monte Carlo simulation of the unpolarized $e^+e^- \to (\pi^+\pi^-)X$ cross section makes the error of n_q negligible.

In the standard Hessian method, the best fit parameters and their 1σ error (corresponding to $\Delta\chi^2 = 1$) at the initial scale $Q_0^2 = 1\ {\rm GeV}^2$ are given in Tab. 3. The χ^2/d.o.f. is 1.23 for the *rigid* scenario, 1.12 for the *flexible* scenario, and 1.26 for the *extra-flexible* scenario. For the 100 replicas, the average χ^2/d.o.f. are 1.35, 1.56 and 1.86, respectively.

4.2 Fitting results

In Fig. 2, the points with error bars represent the transversity combinations for proton (left panel) and deuteron target (right panel) quoted in the last column of Tab. 1. The central value of our best-fit result in the standard approach with the *flexible* scenario is given by the

	HERMES	range	for proton	
Q^2 [GeV^2]	n_u	n_d	n_s	$n_u^{\uparrow}$
1.232	0.607	0.614	0.393	-0.157 ± 0.037
1.604	0.589	0.595	0.380	-0.152 ± 0.037
2.214	0.569	0.575	0.365	-0.146 ± 0.037
4.031	0.536	0.542	0.341	-0.137 ± 0.037
	COMPASS	range	for proton	
Q^2 [GeV^2]	n_u	n_d	n_s	$n_u^{\uparrow}$
1.232	0.897	0.906	0.580	-0.183 ± 0.031
1.476	0.876	0.885	0.565	-0.178 ± 0.031
1.744	0.858	0.867	0.552	-0.175 ± 0.031
2.094	0.840	0.849	0.539	-0.171 ± 0.031
2.802	0.813	0.822	0.520	-0.165 ± 0.031
4.342	0.776	0.785	0.494	-0.158 ± 0.031
6.854	0.742	0.751	0.471	-0.151 ± 0.031
10.720	0.713	0.721	0.451	-0.145 ± 0.031
21.985	0.671	0.679	0.422	-0.136 ± 0.031
	COMPASS	range	for deuteron	
Q^2 [GeV^2]	n_u	n_d	n_s	$n_u^{\uparrow}$
1.253	0.895	0.904	0.578	-0.182 ± 0.031
1.508	0.874	0.883	0.563	-0.178 ± 0.031
1.792	0.855	0.865	0.550	-0.174 ± 0.031
2.266	0.832	0.841	0.534	-0.169 ± 0.031
3.350	0.797	0.806	0.509	-0.162 ± 0.031
5.406	0.759	0.768	0.483	-0.154 ± 0.031
8.890	0.725	0.733	0.459	-0.147 ± 0.031
15.652	0.690	0.698	0.435	-0.140 ± 0.031
33.219	0.650	0.657	0.408	-0.132 ± 0.031

Table 2. The integrated DiFFs according to Eqs. (2.20) and (2.21). The error has been computed at the average Q^2 for each indicated experimental bin.

thick solid line, and it is in good agreement with the data. The error band is the outcome of the merging of all the straight lines connecting the statistical error bars of the fit for each experimental point. The other scenarios do not show significant qualitative differences in the range where data exist.

In Fig. 3, we show the same comparison in the same conditions as in the previous figure, but for the Monte Carlo approach. The band now represents the result of the 68% of all replicas, obtained by rejecting the largest 16% and the lowest 16% of the replicas' values in each x point. We observe no substantial difference between the standard and Monte Carlo approaches.

The resulting transversity distribution is plotted in Fig. 4. The left panel displays the

Rigid scenario			
	up	down	χ^2/d.o.f.
A	0.76 ± 0.35	2.3 ± 2.7	$22.2/18 = 1.23$
B	0.5 ± 2.0	-81 ± 69	
Flexible scenario			
	up	down	χ^2/d.o.f.
A	1.41 ± 0.62	-0.5 ± 6.8	$17.9/16 = 1.12$
B	-11 ± 10	104 ± 413	
C	35 ± 35	$(-22 \pm 54) \times 10^2$	
Extra-flexible scenario			
	up	down	χ^2/d.o.f.
A	1.79 ± 0.53	2.6 ± 5.0	$17.6/14 = 1.26$
B	-24.7 ± 8.7	-239 ± 352	
C	136 ± 53	$(82 \pm 99) \times 10^2$	
D	-183 ± 101	$(-9.2 \pm 10) \times 10^4$	

Table 3. Best-fit parameters and χ^2 values obtained in the standard approach for the three scenarios described in the text and based on Eq. (3.2).

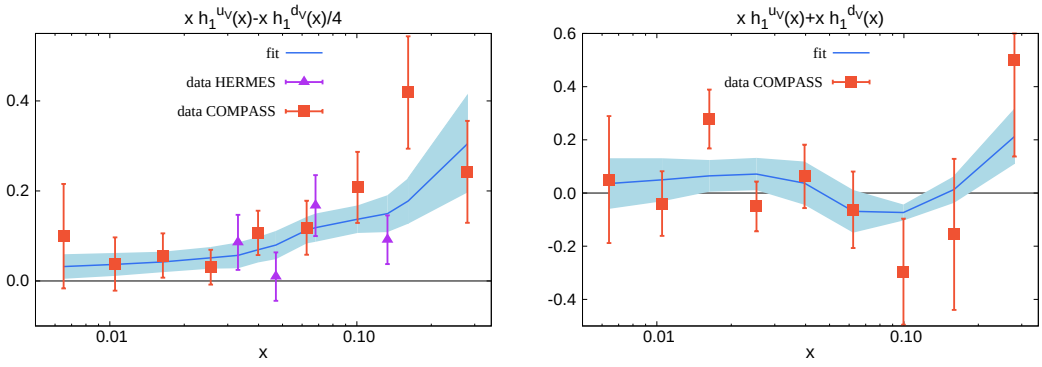

Figure 2. The combinations of Eq. (2.18), left panel, and Eq. (2.19), right panel. The squares and triangles are obtained from the COMPASS and HERMES data, respectively (the values are indicated in the last column of Tab. 1). The thick solid line indicates the central value of the best-fit result in the standard approach with the *flexible* scenario (see text). The error band is the outcome of the merging of all the straight lines connecting the statistical error bars of the fit for each experimental point.

$q = u_v$ contribution in Eq. (3.2), while $q = d_v$ is in the right one. From top to bottom row, the results for the *rigid*, *flexible*, and *extra-flexible*, scenarios are shown, respectively. For each panel, the outcome in the standard approach with the Hessian method is represented by the uncertainty band with solid boundaries, the central thick solid line visualizing the central value. The partially overlapping band with dashed boundaries is the outcome when adopting the Monte Carlo approach, where the band width corresponds to the 68% of all the 100 replicas, again produced as before by rejecting the largest 16% and the lowest

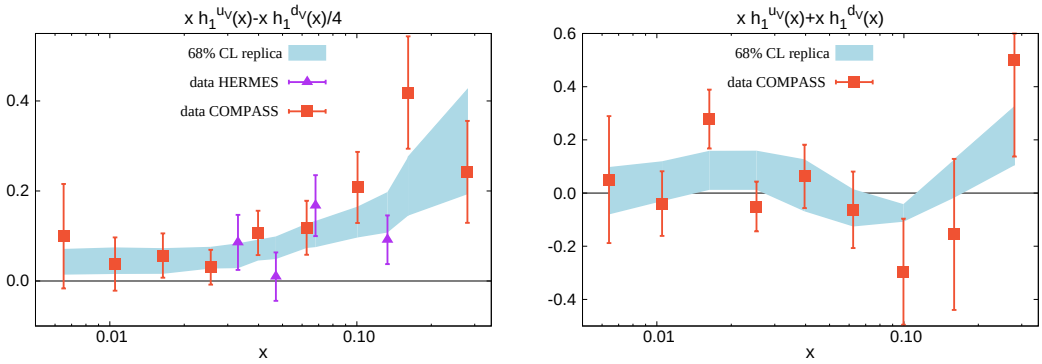

Figure 3. Same observables and data symbols as in the previous figure. The uncertainty band represents in the Monte Carlo approach the selected 68% of all fitting replicas (see text).

16% among the replicas' values in each x point. As such, the set of selected replicas in the 68% band can change in each different x point; consequently, the band itself can show some irregular wiggles. For sake of comparison, each panel displays also the corresponding results for the only other existing parametrization available [**?**], depicted as a band with short-dashed boundaries. Since the latter was extracted at the scale $Q^2 = 2.4$ GeV^2, our results are properly evolved at the same scale. Finally, the dark thick solid lines indicate the Soffer bound, also evolved at the same scale $Q^2 = 2.4$ GeV^2 (using LO evolution as in the rest of the analysis).

For the *flexible* scenario (middle row of Fig. 4), the uncertainty bands in the standard and Monte Carlo approaches are quite similar. The main difference is that in the former case the boundaries of the band can occasionally cross the Soffer bound. This is due to the fact that the assumed quadratic dependence of χ^2 on the parameters around its minimum is not a reliable one, when getting close to the bounds. On the contrary, in the Monte Carlo approach each replica is built such that it never violates the Soffer bound; the resulting 68% band is always within those limits.

For the valence up contribution (left panel), the standard approach tends to saturate the Soffer bound at $x \sim 0.4$ (outside the range where data exist). In the Monte Carlo approach, some of the replicas saturate the bound already at lower values. However, there are also a few replicas that do not saturate the bound at all, or even saturate the lower Soffer bound. These replicas typically fall outside the 68% band drawn in the figures. Nevertheless, they can still have a good χ^2 when compared to the data.

For the down valence contribution (right panel), both approaches saturate the lower limit of the Soffer bound already at $x \sim 0.1$, i.e. in a region where data exist. This behavior is driven by the data, in particular by the bins number 7 and 8 in the deuteron measurement. No such trend is evident in the corresponding single-hadron measurement of the Collins effect, from which the other parametrization of Ref. [**?**] is extracted. As a matter of fact, this is the only source of significant discrepancy between the two extractions, which otherwise show a high level of compatibility despite the fact that they are obtained from very different procedures. Note that if the Soffer bound is saturated at some scale, it

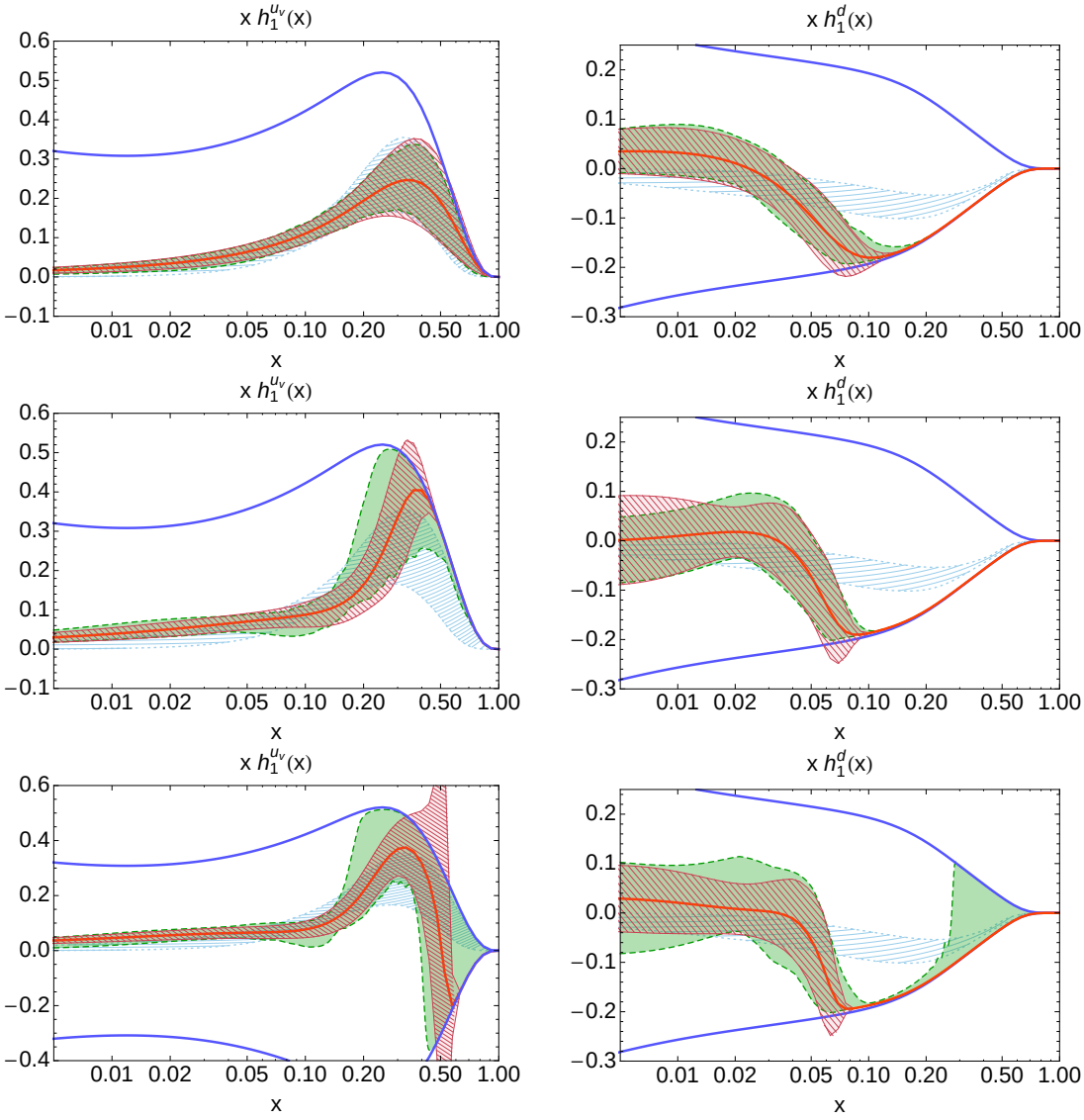

Figure 4. The up (left) and down (right) valence transversities coming from the present analysis evolved to $Q^2 = 2.4$ GeV^2. From top row to bottom, results with the *rigid*, *flexible*, and *extra-flexible* scenarios are shown, respectively. The dark thick solid lines are the Soffer bound. The uncertainty band with solid boundaries is the best fit in the standard approach at 1σ, whose central value is given by the central thick solid line. The uncertainty band with dashed boundaries is the 68% of all fitting replicas obtained in the Monte Carlo approach. As a comparison, the uncertainty band with short-dashed boundaries is the transversity extraction from the Collins effect [**?**].

is likely to be significantly violated at a lower scale [**?**]. Therefore, if we want to maintain the validity of the Soffer bound at $Q^2 < 1$ GeV^2, we would expect transversity to be clearly below the Soffer bound at $Q^2 \geq 1$ GeV^2. In fact, in our analysis with the Monte Carlo approach there are a few replicas that do not saturate the Soffer bound. They fall outside the 68% band drawn in the figure, but they are still compatible with the data due to the large experimental error bars (this is true in particular for the deuteron bins number 7 and

8). Therefore, at present we cannot conclude that the the Soffer bound is saturated or violated, even though the fit seems to point in that direction. We mention that interesting speculations concerning violations of the Soffer bound were presented in Ref. [**?**].

At low x, the functional form in the *flexible* scenario tends to zero by construction, and similarly in all other scenarios. However, the behavior down to $x \sim 0.005$ is driven by data. In fact, the functional form can have up to two nodes in $x \in [0, 1]$. In the Monte Carlo approach, most of the replicas for $xh_1^{u_v}$ have no node, while for $xh_1^{d_v}$ have one or even two nodes.

In the *rigid* scenario (upper row in Fig. 4), most of the features are similar to the *flexible* scenario in the region where data exist, but there are some differences outside that range. For the valence up quark (left panel), both standard and Monte Carlo approaches give uncertainty bands that saturate the Soffer bound at higher x, almost completely overlapping with the result obtained from the Collins effect. For the valence down quark (right panel), the trend is very similar to the *flexible* scenario: the parametrization saturates the lower Soffer bound at $x \gtrsim 0.1$. This demonstrates that this unexpected behavior is not an artefact of the functional form, but is due to the experimental data. In the Monte Carlo approach, the majority of replicas show the same behavior, but a few ones (falling outside the 68% band) do not, again as in the *flexible* scenario.

Finally, for the *extra-flexible* scenario (bottom row in Fig. 4) the distinction between regions with and without experimental data is even more clear. Where there are data, the results are highly compatible with the other scenarios. But at $x \gtrsim 0.4$ for the u_v case (left panel), the uncertainty band in the standard approach substantially violates the Soffer bound. This is an artefact of the assumptions used in error propagation, together with the lack of data at high x. In the Monte Carlo approach, the replicas entirely fill the area between the upper and lower Soffer bound, both for the up quark at $x \gtrsim 0.4$ and for the down quark at $x \gtrsim 0.25$. This is an explicit visualization of the realistic degree of uncertainty about transversity in the x range where there are no experimental data points.

We have explored other scenarios for the transversity functional form. We tried different arguments in the hyperbolic tangent, specifically different powers in the first factor, but with no significant change for $x \gtrsim 0.01$. Using the $x^{1/4}$ factor, the error band at low x becomes considerably wider. The valence transversities remain integrable, but stable values of the tensor charge can be reached only by pushing the lower limit in the integral to extremely small values $x \lesssim 10^{-10}$ (see below).

A qualitative comparison between the results of the present work and the available model predictions can be done using the results collected in Ref. [**?**]. In particular, we note that the extracted transversity for the up quark is smaller than most of the model calculations at intermediate $x \in [0.1,\ 0.2]$, while it is larger at lower x ($x \sim 0.01$). The down transversity is much larger in absolute value than all model calculations at intermediate x (as observed before, this is due to the deuterium data points), while the error band is too large to draw any conclusion at lower x.

Transversity is directly related to the tensor charge, a fundamental quantity of hadrons at the same level as the vector, axial, and scalar charges. The tensor charge remains at the moment largely unconstrained. It can be directly compared with lattice QCD predictions

	δu	δd	δu	δd
$Q_0^2 = 1$ GeV^2	$x \in [0.0064, 0.28]$	$x \in [0.0064, 0.28]$	$x \in [0, 1]$	$x \in [0, 1]$
Standard rigid	0.30 ± 0.09	-0.26 ± 0.17	0.57 ± 0.21	-0.18 ± 0.33
MC rigid	0.30 ± 0.07	-0.22 ± 0.11	0.56 ± 0.12	-0.08 ± 0.27
Standard flex.	0.29 ± 0.13	-0.26 ± 0.22	0.72 ± 0.24	-0.33 ± 0.61
MC flex.	0.32 ± 0.09	-0.24 ± 0.11	0.77 ± 0.22	-0.45 ± 0.48
Standard extra-flex.	0.32 ± 0.12	-0.25 ± 0.15	0.61 ± 0.40	-0.16 ± 0.44
MC extra-flex.	0.34 ± 0.10	-0.20 ± 0.14	0.68 ± 0.22	-0.12 ± 0.69

Table 4. Table of the results for the tensor charge at $Q_0^2 = 1$ GeV, truncated in the range where data exist (second and third column) and extended to the whole x range (third and fourth column). The results are given for the standard and Monte Carlo approach and for the three scenarios considered in the fit.

(see, *e.g.*, Refs. [**?** **?**]) or models (see, *e.g.*, Refs. [**?** **?** **?** **?** **?**]). There is no sum rule related to the tensor current, due to the property of the anomalous dimensions governing the QCD evolution of transversity. The contribution of a flavor q to the tensor charge is defined as

$$\delta q(Q^2) = \int dx\, h_1^{q_v}(x; Q^2)\ . \tag{4.1}$$

The region of validity of our fit is restricted to the experimental data range. We can therefore give a reliable estimate for the tensor charge truncated to the interval $x \in [0.0064, 0.28]$. In the first two columns from left of Tab. 4 we list the results obtained in the different approaches and scenarios. We tried also to extend the range of integration outside the experimental data to $x \in [0, 1]$. The result is heavily influenced by the adopted functional form, in particular by the low-x exponent. Nevertheless, we quote our result in the last two columns of Tab. 4.

Our results for the tensor charges in the *flexible* scenario are slightly larger in absolute value compared to the ones in Ref. [**?**]. They are compatible within errors. Results obtained in several models can be found in, *e.g.*, Refs. [**?** **?** **?**]. As emphasized in Ref. [**?**], care must be taken when comparing results at different scales. The ratio between the up and down tensor charges is scale invariant. The values we obtain in all our scenarios are compatible with all models within the large errors. In order to better determine the tensor charge, more data at high and low x are needed.

5 Conclusions and Outlook

The transversity parton distribution function (PDF) is an essential missing piece of our knowledge on the proton at leading-twist. It is a chiral-odd object, whose Q^2 dependence obeys the non-singlet QCD evolution. Its integral over x is related to the nucleon tensor charge. Positivity bounds constrain its absolute value to be smaller than the absolute value of the number density and helicity, the so-called Soffer bound. Due to its chiral-odd nature, transversity cannot be accessed in fully inclusive deep-inelastic scattering. It is however

possible to access it in two-particle-inclusive DIS [**?** **?** **?**] in combination with Dihadron Fragmentation Functions (DiFFs).

In this paper, we have obtained for the first time the parameterization of the up and down valence transversities based on a collinear framework, using data for $\pi^+\pi^-$ semi-inclusive DIS off transversely polarized targets from the HERMES and COMPASS collaborations [**?** **?**], combined with the Belle data on almost back-to-back emission of two $\pi^+\pi^-$ pairs in e^+e^- annihilations [**?**]. We have explored different scenarios for the functional form, all subject to the theoretical constraint of the Soffer bound [**?** **?**]. We have also performed the error analysis in two independent ways. The first one is a standard one based on the Hessian method. The second one is based on the random generation of a large number of replicas of the experimental points, and on the fit of each of these replicas, producing an envelope of trajectories whose spread is the generalization of the 1σ uncertainty band when the distribution is not necessarily a Gaussian. As such, the second method is more reliable particularly when the fitting curves hit the Soffer bound, and the χ^2 function cannot be expected to have the quadratic dependence on the fit parameters as required by the Hessian method. Nevertheless, in the kinematical range of the experimental measurements the two methods give almost overlapping results in all explored scenarios.

In the range where data exist, our results are compatible with the only other existing parametrization of transversity, which is determined from the Collins effect in single-hadron SIDIS off transversely polarized targets [**?**]. The only source of discrepancy lies in the range $0.1 \lesssim x \lesssim 0.16$ for the valence down quark, where two experimental data for the deuteron target drive our fitting curves to saturate the lower Soffer bound. However, the large error bars of these two points prevent us from drawing any conclusion about a possible violation of the Soffer inequality.

Outside the kinematical range of experiments, the lack of data reflects itself in a large uncertainty in the parametrization. For the *extra-flexible* scenario and the error analysis based on the random approach, the replicas take all the available values between the upper and lower Soffer bound at large x. This illustrates in a very effective way the need for new large$-x$ data in order to reduce the degree of uncertainty in the knowledge of transversity.

In the near future, more data are expected from the HERMES and COMPASS collaborations. They will include also different types of hadron pairs (e.g., $K\pi$), which should allow us to improve the flavour separation of transversity. Two-particle inclusive DIS will be measured also at JLab in the future, which should considerably increase our knowledge of transversity at high x. Finally, invaluable information will come also from polarized proton-proton collisions [**?**]: data are expected from the PHENIX and STAR collaborations (see, e.g., [**?**]).

Acknowledgments

We are grateful to Marco Guagnelli for providing us with a modified version of the HOPPET evolution code. We acknowledge useful discussions with Andrea Bianconi, Stefano Melis, and Emanuele Nocera. A. Courtoy is working under the Belgian Fund F.R.S.-FNRS via the contract of Chargée de recherches. This work is partially supported by the Italian MIUR

through the PRIN 2008EKLACK, and by the Joint Research Activity “Study of Strongly Interacting Matter" (acronym HadronPhysics3, Grant Agreement No. 283286) under the 7th Framework Programme of the European Community.

A Appendix

For convenience, we reproduce here the explicit analytic forms of the Soffer bound used in our analysis, which is based on the MSTW08LO set [**?**] for the unpolarized PDF, combined to the DSSV parameterization [**?**] for the helicity distribution. The equations hold at $Q_0^2 = 1$ GeV^2.

$$x\mathrm{SB}^u(x) + x\mathrm{SB}^{\bar{u}}(x) = \frac{1}{2}\Big[xf_1^{u_v}(x) + 2xf_1^{\bar{u}}(x) + xg_1^u(x) + xg_1^{\bar{u}}(x)\Big], \tag{A.1}$$

$$xf_1^{u_v}(x) = 1.4335x^{0.45232}(1-x)^{3.0409}\left(1 + 8.9924x - 2.3737\sqrt{x}\right), \tag{A.2}$$

$$\begin{aligned} 2xf_1^{\bar{u}}(x) = \frac{1}{2}\Big[&\left(1 + 16.865x - 2.9012\sqrt{x}\right) \\ &\times \frac{0.59964(1-x)^{8.8801} - 0.10302(1-x)^{13.242}}{x^{0.16276}} \\ &- 17.8826x^{1.876}(1-x)^{10.8801}\left(1 - 36.507x^2 + 8.4703x\right)\Big], \end{aligned} \tag{A.3}$$

$$xg_1^u(x) + xg_1^{\bar{u}}(x) = 0.677x^{0.692}(1-x)^{3.34}\left(1 + 15.87x - 2.18\sqrt{x}\right), \tag{A.4}$$

$$x\mathrm{SB}^d(x) + x\mathrm{SB}^{\bar{d}}(x) = \frac{1}{2}\Big[xf_1^{d_v}(x) + 2xf_1^{\bar{d}}(x) + xg_1^d(x) + xg_1^{\bar{d}}(x)\Big], \tag{A.5}$$

$$xf_1^{d_v}(x) = 5.0903x^{0.71978}(1-x)^{5.1244}\left(1 + 7.473x - 4.3654\sqrt{x}\right), \tag{A.6}$$

$$\begin{aligned} 2xf_1^{\bar{d}}(x) = &\, 2xf_1^{\bar{u}}(x) \\ &+ 17.8826x^{1.876}(1-x)^{10.8801}\left(1 - 36.507x^2 + 8.4703x\right), \end{aligned} \tag{A.7}$$

$$xg_1^d(x) + xg_1^{\bar{d}}(x) = -0.015x^{0.164}(1-x)^{3.89}\left(1 + 98.94x + 22.4\sqrt{x}\right). \tag{A.8}$$

References